RSC Advances

PAPER

View Article Online
View Journal | View Issue

Check for updates

Cite this: *RSC Adv.*, 2026, **16**, 29918

Superior electrochemical performances of highly porous bismuth oxyhalides decorated lemon peel derived activated carbon electrode materials for solid state asymmetric and symmetric supercapattery devices

Bhuvaneshwari Ramasamy,[a] Jeya M. Peter Paul,[a] Kannan Raman[b] and Rajashabala Sundaram*[a]

Received 8th April 2026
Accepted 18th May 2026

DOI: 10.1039/d6ra02955h

rsc.li/rsc-advances

The ever-increasing energy demand and rapid growth of modern industries enforce the scientific community to search for alternative renewable energy resources. To overcome the energy crisis, a hybrid electrochemical energy storage device, namely, supercapattery, is considered a promising green energy source as it combines the merits of supercapacitors and batteries. The present work deals with the electrochemical performance of bismuth oxyhalide/lemon peel-derived activated carbon (BOX-LPDAC, X = bromine, chlorine, or iodine) electrode materials for supercapattery applications. The highly porous sheet-like morphology of the prepared electrode materials promotes more charge storage of electrolytic ions during the electrochemical reaction. Moreover, the BOB-LPDAC (1575.15 C g^{-1}), BOC-LPDAC (1228 C g^{-1}) and BOI-LPDAC (905.37 C g^{-1}) electrodes have high specific capacity than bare BOB (646.75 C g^{-1}), BOC (530.91 C g^{-1}), BOI (409.57 C g^{-1}) and LPDAC (165.19 C g^{-1}) electrodes due to the presence of synergistic battery-type faradaic (BOX) and capacitive-type (LPDAC) charge storage mechanisms. The fabricated solid-state symmetric supercapattery (BOB-LPDAC‖BOB-LPDAC) (SSC) device could deliver an energy density of 172.06 Wh kg^{-1} than the asymmetric supercapattery (BOB-LPDAC‖LPDAC) (ASC) device (47.1 Wh kg^{-1}). Compared to the ASC device, the SSC device could power a 2 V red LED for 555 s and a 3.7 V electric motor fan for 122 s. Hence, the prepared BOB-LPDAC nanocomposite may serve as an excellent electrode material for solid-state symmetric supercapattery applications.

1 Introduction

The burgeoning population and increasing energy demand have led to a transition from non-renewable energy sources to environmentally friendly renewable energy sources.[1–3] The existing renewable energy sources, such as solar, wind and tidal energies, have the demerit of weather-dependent energy supply.[2,4] Therefore, renewable electrochemical energy storage (EES) systems such as batteries and supercapacitors have become a hot topic.[5] So far, neither supercapacitors nor rechargeable batteries have the ability to revolutionize the renewable energy industry remarkably. Recently, a hybrid EES namely supercapattery, has attracted the scientific community owing to its synergistic characteristics that combine the merits of energy density from battery-type electrode materials and power density from supercapacitor-type electrode materials.[6,7]

A variety of electrode materials, including transition metal oxides (TMOs), transition metal sulphides (TMSs), transition metal phosphates (TMPs) and carbon-based materials have been utilized for supercapattery applications.[8] Even though TMO-based supercapattery devices, such as $NiCuCo_2O_4$‖luffa sponge-derived activated carbon [65 Wh kg^{-1}; 500 W kg^{-1}][9] and $MnCo_2O_4$‖AC[7] [33.8 Wh kg^{-1}; 318.9 W kg^{-1}], deliver high energy density, their practical applicability is restricted due to low power density. In the case of TMS-based supercapattery devices, Mn-CoS‖AC [17.94 Wh kg^{-1}; 806 W kg^{-1}][10] and $Zn_{0.5}Co_{0.5}S$‖AC [49 Wh kg^{-1}; 957 W kg^{-1}][11] deliver high energy density but suffer from low electrochemical stability.[12,13] On the contrary, TMP-based supercapattery devices, such as $Cu_3(PO_4)_2$‖AC [65.96 Wh kg^{-1}; 750 W kg^{-1}][6] and $Co_3(PO_4)_2$/GO‖AC [82.69 Wh kg^{-1}; 433.33 W kg^{-1}],[14] offer high cyclic stability but poor rate capability.[15,16] Hence, these transition metal-based electrode materials could not find their place in the realm of supercapattery applications.

---

[a] *Computational Modelling and Energy Harvesting Laboratory, School of Physics, Madurai Kamaraj University, Madurai 625021, India. E-mail: rajashabala.physics@mkuniversity.ac.in; rajashabala@yahoo.com*

[b] *Department of Physics, Anna University Regional Campus, Madurai, Tamil Nadu, 625019, India*

Nowadays, bismuth (Bi)-based electrodes bloom the electrochemical energy storage industries due to their faradaic redox reactions, tunable morphology, good chemical stability and environment-friendly nature.[17,18] Theoretical studies on Bi-based compounds reveal that the dendrite-free 3-electron redox conversion of Bi^{3+}/Bi pair offers a high specific capacity of 384 mAh g^{-1}.[19] Recently, the bismuth manganese oxide ($BiMnO_3$)||AC asymmetric supercapacitor device exhibited an energy density of 14.4 Wh kg^{-1} and a very low power density of 50 W kg^{-1} at a current density of 0.00025 A cm^{-2},[20] whereas the bismuth iron manganese oxide ($Bi_2Fe_2Mn_2O_{10}$)||AC delivered a high energy density of 48 Wh kg^{-1} and a low power density of 480 W kg^{-1} at a current density of 0.6 A g^{-1}.[2] The bismuth oxide (Bi_2O_3)/ferric sulfide (FeS)||AC asymmetric device delivered an energy density of 15 Wh kg^{-1} and a low power density of 590 W kg^{-1} at a current density of 1 A g^{-1}.[21] The bismuth–copper oxide (Bi_2CuO_4)||AC solid-state flexible asymmetric device offers an energy density of 55.3 Wh kg^{-1} and a power density of 4570 W Kg^{-1} at a current density of 0.01 A cm^{-2} but retained only 78.2% of its initial capacity after 5000 cycles.[22]

Even though a variety of electrode materials have been utilized, none of them are better electrochemical materials for EES applications. The electrochemical performance of the prepared electrodes mainly relies on energy density, power density, electrical conductivity and cyclic stability. Bismuth oxyhalides (BOX) are considered effective battery-grade electrode materials owing to their layered structure and multi-electron transfer nature.[23,24] BOX are V–VI–VII group ternary materials that consist of alternatively arranged tetragonal matlockite-type $[Bi_2O_2]^{2+}$ layers stacked between two slabs of halogen (X^-) ions.[24,25] In addition, the presence of corridors in the interlayer acts as active sites for the electrolyte ions to intercalate/deintercalate, facilitating the electrolyte ions to participate in the faradaic reaction at the Bi sites.[17,19]

Carbonaceous materials (graphene oxide (GO), reduced graphene oxide (rGO), graphitic carbon nitride ($g\text{-}C_3N_4$) and activated carbon (AC)) are believed to be the power source in supercapattery applications due to their electric double layer capacitor (EDLC)-type charge storage mechanism.[6,8,26] In particular, biomass-derived activated carbon (BAC) from plants and animals is considered a promising electrode material because of its high surface area (>1000 m^2 g^{-1}), high conductivity, excellent chemical stability, high porosity (>0.5 cm^3 g^{-1}), low cost, earth abundance and ease of production.[27–31] These properties of BAC favour high power density and more capacity retention rate for supercapattery applications.[32,33]

The present work† deals with a systematic investigation on the electrochemical performance of three different electrode materials, namely, bismuth oxybromide/lemon peel derived activated carbon (BOB-LPDAC), bismuth oxychloride/lemon peel derived activated carbon (BOC-LPDAC) and bismuth oxyiodide/lemon peel derived activated carbon (BOI-LPDAC), towards high performance solid-state supercapattery applications. A facile ultrasonication method was adopted for the preparation of the BOB-LPDAC, BOC-LPDAC and BOI-LPDAC nanocomposite electrode materials. The prepared supercapattery electrode materials were subjected to cyclic voltammetry and galvanostatic charge–discharge studies for the confirmation of battery-type charge storage mechanism of BOX and capacitive-type behaviour of LPDAC. Supreme solid-state asymmetric and symmetric supercapattery devices using BOB-LPDAC and LPDAC electrodes will be fabricated to achieve the United Nations sustainable development goal (SDG) 2030. Moreover, the practical applicability of the fabricated solid-state asymmetric and symmetric supercapattery devices will be tested to power a commercial red light-emitting diode (LED) and an electric motor fan.

2 Experimental methods

2.1 Synthesis of bismuth oxyhalides (BOX (X = bromine, chlorine, and iodine))

A co-precipitation method was adopted for the synthesis of BOX nanomaterials (see SI 1.2), and the schematic representation for the preparation of BOX is provided in Fig. S1.

2.2 Preparation of the biomass-derived activated carbon from lemon peel (LPDAC)

A chemical activation method followed by pyrolysis was used to prepare LPDAC (see SI 1.3 and Fig. S2).

2.3 Synthesis of bismuth oxyhalide-lemon peel derived activated carbon (BOX-LPDAC) nanocomposites as electrode materials

The BOX-LPDAC nanocomposites were prepared using a facile ultrasonication method (see SI 1.4 and Fig. S3).

2.4 Preparation of PVA/KOH solid-state electrolyte

In order to fabricate the solid-state supercapattery device, the PVA/KOH solid-state electrolyte was prepared using the solution casting method (see SI 1.5).

3 Results and discussions

3.1 XRD analysis

The crystallinity and grain size of the prepared BOB, BOC, BOI, LPDAC, BOB-LPDAC, BOC-LPDAC and BOI-LPDAC nanomaterials were analyzed using XRD analysis. Fig. S4(a) shows the diffraction peaks of BOB at 10.57°, 21.39°, 24.91°, 31.39°, 31.90°, 39.02°, 46.02°, 50.39°, 53.23° and 56.91°, which correspond to the (001), (002), (101), (102), (110), (112), (200), (104), (211) and (212) planes, respectively.[34,35] All these peaks were well matched with the JCPDS card no. 09-0393 and exhibits the tetragonal phase of BOB with lattice constants of a, $b = 3.91$ Å and $c = 8.14$ Å.[36,37]

The prepared BOC has the diffraction peaks at $2\theta = 11.80°$, 24.08°, 25.98°, 32.79°, 33.47°, 40.82°, 46.86°, 49.70°, 54.49° and 58.77°, which correspond to the *hkl* planes of (001), (002), (101), (110), (102), (112), (200), (113), (211) and (212), respectively.

---

† This is the republication of an article previously retracted [https://pubs.rsc.org/en/content/articlelanding/2026/ra/d6ra90026g] when published by the incorrect authors.

These peaks coincide well with the JCPDS card no. 06-0249 and reveal the tetragonal phase of BOC (a, $b = 3.87$ Å and $c = 7.38$ Å) (see Fig. S4(b)).[38] BOI has the prominent diffraction peaks at $2\theta = 9.47°$, 29.29°, 31.78°, 45.59° and 55.23°, which denote the crystal planes of (001), (102), (110), (200) and (212), respectively (see Fig. S4(c)). These characteristic peaks well match with the JCPDS card no. 10-0445 and indicate the tetragonal phase of BOI with a, $b = 3.98$ Å and $c = 9.11$ Å.[39,40] In the case of LPDAC, two broad peaks appeared at 25.32° and 43.42° indexed to the (002) and (101) *hkl* planes, respectively, and agree well with the JCPDS card no. 41-1487 (see Fig. S4(d)).[41,42] Moreover, these broad diffraction peaks of LPDAC confirm its amorphous nature.[43]

All the diffraction peaks of BOB, BOC and BOI were also observed in the prepared BOB-LPDAC, BOC-LPDAC and BOI-LPDAC nanocomposites, respectively (see Fig. 1(a–c)). It is clear that the tetragonal crystal phase is maintained for BOB, BOC and BOI even after the addition of LPDAC in the prepared nanocomposites.[44] In addition, no characteristic diffraction peaks of LPDAC were present in these nanocomposites, which may due to the weak diffraction intensity of the activated carbon.[43] The reduction in peak intensity at 31.90° of BOB, 33.47° of BOC and 31.78° of BOI due to the addition of LPDAC confirms the presence of LPDAC at the surface of BOB, BOC and BOI, respectively.[39,45]

The grain size (GS) and crystallinity (%) of the prepared BOB, BOC, BOI, BOB-LPDAC, BOC-LPDAC and BOI-LPDAC electrode materials are calculated using the following formulae, respectively (see Table S1).[46,47]

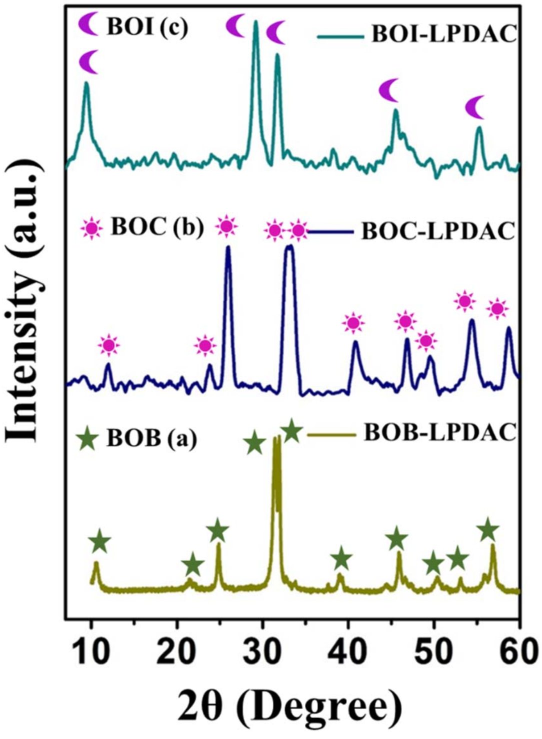

Fig. 1 XRD patterns of the prepared (a) BOB-LPDAC, (b) BOC-LPDAC and (c) BOI-LPDAC electrode materials.

$$\text{Grain size(GS)} = \frac{0.9\lambda}{\beta\cos(\theta)}(\text{nm}), \tag{1}$$

$$\text{Crystallinity}(\%) = \left[\frac{\text{crystalline area}}{\text{overall area}}\right] \times 100, \tag{2}$$

where λ is the wavelength of the X-ray, β is the fullwidth at half maximum (FWHM) and θ is the diffraction angle.

The reduction in the grain size and crystallinity of the prepared BOB-LPDAC, BOC-LPDAC and BOI-LPDAC nanocomposites is due to the addition of amorphous LPDAC into crystalline BOB, BOC and BOI, respectively.[36] From the XRD results, it is observed that among the prepared nanocomposites, BOB-LPDAC has the least crystallite size of 11.03 nm and high crystallinity of 77.38%. The high crystallinity of the BOB-LPDAC electrode material promotes efficient faradaic redox reactions and facilitates easy ion transport owing to its shorter diffusion path length.[48] These outcomes suggest that the prepared BOB-LPDAC nanocomposite may serve as a better electrode material compared to the BOC-LPDAC and BOI-LPDAC nanocomposites for supercapattery applications.

3.2 FESEM analysis

The surface morphology of the prepared BOB, BOC, BOI, LPDAC, BOB-LPDAC, BOC-LPDAC and BOI-LPDAC electrode materials are shown in Fig. S6 and 2. In the present work, a nanosheet-like morphology for BOB, an irregular nanosheet-like morphology for BOC, a nanoflake-like morphology for BOI and a sheet-like morphology with high degree of porosity for LPDAC were observed (see Fig. S6(a–d)).[49,50] The presence of more pores in the prepared LPDAC due to chemical activation by KOH may enhance the specific surface area and provide efficient pathways for ion insertion and exertion.[51–53] The ultrasonically derived BOB-LPDAC nanocomposite reveals that the highly porous nature of LPDAC may accommodate more BOB nanosheets (see Fig. 2(a)). In the case of the BOC-LPDAC nanocomposite, the BOC nanosheets are decorated at the surface of LPDAC (see Fig. 2(b)), whereas in BOI-LPDAC, the BOI nanoflakes are decorated at the surface of LPDAC (see Fig. 2(c)). Among all the three nanocomposites, BOB-LPDAC has the highly porous LPDAC nanosheets, which can enhance electrolyte ion storage and facilitate more charge transfer during the electrochemical reaction.[27,52]

3.3 HRTEM analysis

The crystalline nature and morphology of the prepared BOB, BOC, BOI, LPDAC, BOB-LPDAC, BOC-LPDAC and BOI-LPDAC electrode materials were confirmed from HRTEM characterization.[54] Fig. S9(a and b) reveals the sheet-like morphology of the prepared BOB and BOC, whereas BOI exhibits a flake-like morphology with sharp edges (see Fig. S9(c)). In addition, BOB, BOC and BOI have an interplanar lattice spacing of 0.28 nm, 0.27 nm and 0.28 nm, corresponding to the d_{110} plane, respectively.[55–57] From Fig. S9(d), it is evident that the prepared LPDAC is highly porous in nature.[28] Furthermore, the absence of lattice spacing in LPDAC authenticates its amorphous

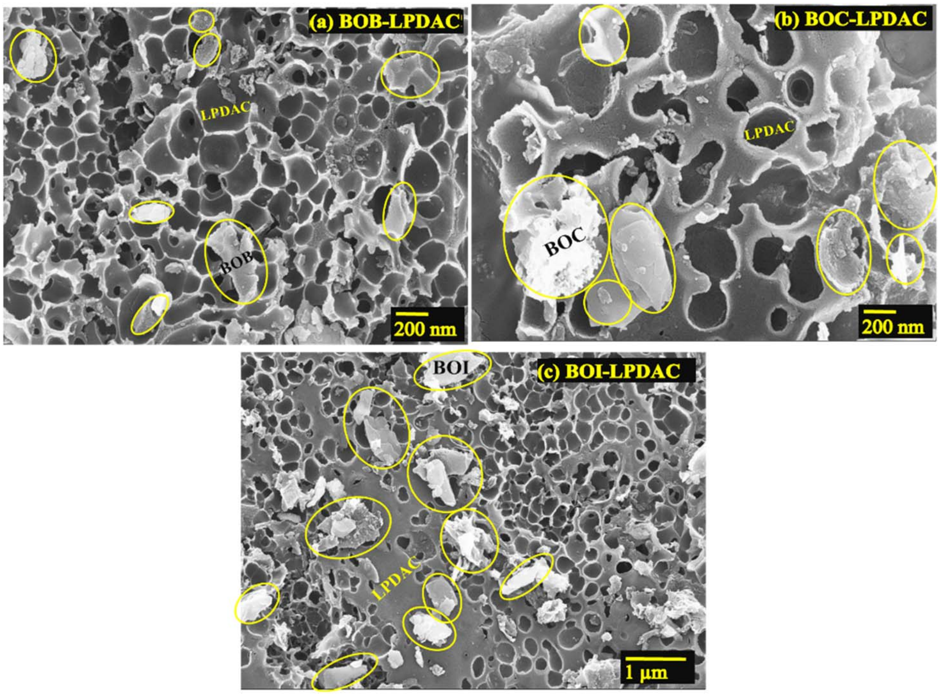

Fig. 2 FESEM images of the (a) BOB-LPDAC, (b) BOC-LPDAC and (c) BOI-LPDAC electrode materials.

Table 1 Anodic and cathodic peaks of the prepared BOB, BOC and BOI electrodes

	Anodic peaks (V)		Cathodic peak (V)
Electrodes	O1	O2	R1
BOB	−0.52	−0.31	−0.76
BOC	−0.48	−0.27	−0.79
BOI	−0.59	−0.39	−0.89

nature.[41] In the case of the BOB-LPDAC and BOC-LPDAC nanocomposites, butterfly-shaped BOB/BOC nanosheets were embedded at the surface of the amorphous LPDAC (see Fig. S9(e and f)),[27] where the BOI-LPDAC nanocomposite indicates that the BOI nanoflake was decorated at the surface of LPDAC (see Fig. S9(g)). These findings well supported the results obtained from the XRD and FESEM studies.

3.4 BET analysis

The specific surface area of the prepared BOB, BOC, BOI, LPDAC, BOB-LPDAC, BOC-LPDAC and BOI-LPDAC electrode materials was analysed using a Brunauer–Emmett–Teller (BET) study (see Fig. S10 and Table S3).[58] The addition of LPDAC (1610 $m^2 g^{-1}$) to BOB, BOC and BOI greatly increases the specific surface area from 18.19 $m^2 g^{-1}$, 16.12 $m^2 g^{-1}$ and 11.80 $m^2 g^{-1}$ to 981 $m^2 g^{-1}$, 783 $m^2 g^{-1}$ and 610 $m^2 g^{-1}$ for the prepared nanocomposites of BOB-LPDAC, BOC-LPDAC and BOI-LPDAC, respectively.[36] The increase in specific surface area ensures the decoration of BOB/BOC/BOI at the surface of the highly porous LPDAC.[41] The calculated pore size of 2.98 nm, 3.32 nm, 2.94 nm, 2.52 nm, 2.38 nm, 2.70 nm and 2.74 nm, respectively, for the prepared BOB, BOC, BOI, LPDAC, BOB-LPDAC, BOC-LPDAC and BOI-LPDAC electrode materials using Barrett–Joyner–Halenda (BJH) ensures that all the prepared electrode materials are mesoporous nature.[36] Among all the prepared nanocomposites, the BOB-LPDAC has favourable properties of high specific surface area (981 $m^2 g^{-1}$), large pore volume (0.583 nm) and less pore size (2.38 nm) and thereby it can offer more adsorption sites to store more electrolyte ions for the enhanced electrochemical energy storage performance.[59,60]

3.5 TGA study

The thermal stability and humidity of the prepared BOB, BOC, BOI, LPDAC, BOB-LPDAC, BOC-LPDAC and BOI-LPDAC electrode materials were investigated using thermogravimetric analysis under an N_2 atmosphere (see Fig. S11).[61] The TGA curve of BOB shows three stages of weight loss, whereas the BOC and BOI exhibit significant weight loss in four stages (see Fig. S11(a)).[62] In addition, LPDAC undergoes a two-stage weight loss, while the BOB-LPDAC, BOC-LPDAC and BOI-LPDAC nanocomposites indicate a three-stage weight loss (see Fig. S11(b)). The first weight loss around 200 °C is due to the evaporation of water molecules in the prepared BOB, BOC, BOI, BOB-LPDAC, BOC-LPDAC and BOI-LPDAC electrode materials.[59] From Table S4, it is evident that the thermal decomposition of BOX into bismuth monoxide (BiO) and X_2 occurs at 667 °C (BOB), 562 °C (BOC) and 448 °C (BOI), respectively (see eqn (3)).[62,63]

$$2BOX \rightarrow 2BiO + X_2 \quad (3)$$

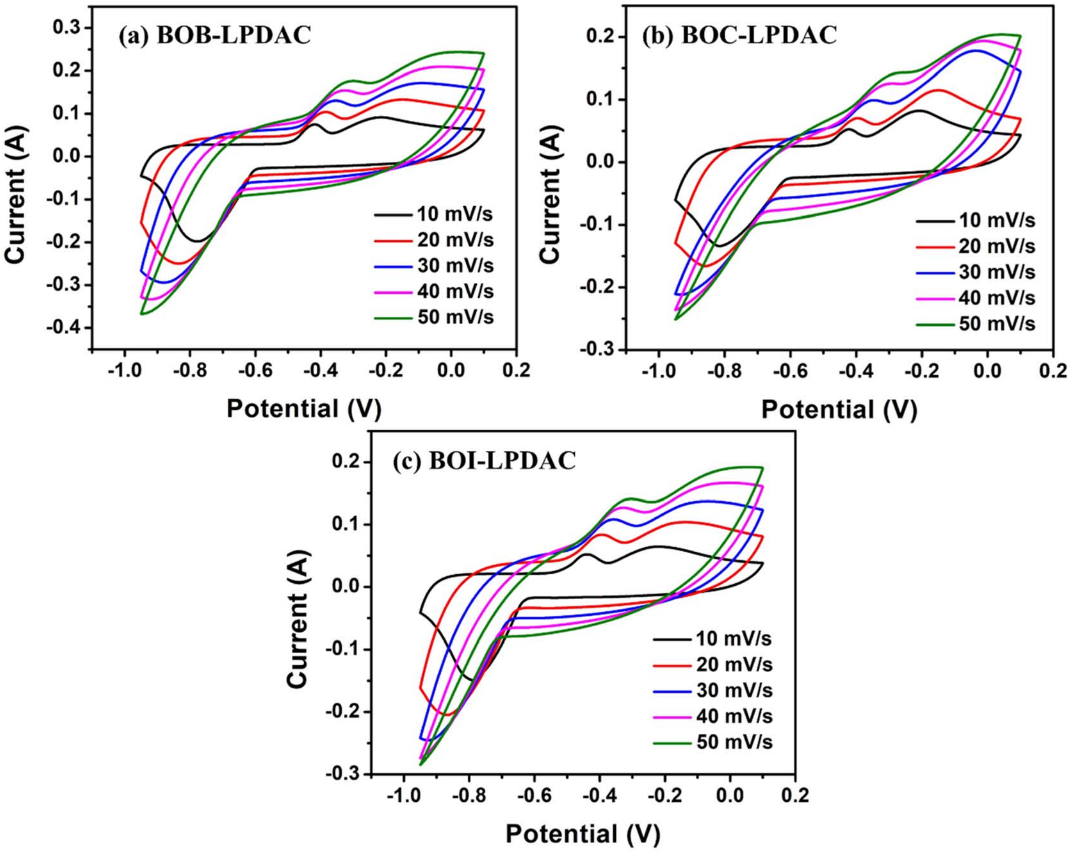

Fig. 3 CV curves at different scan rates for the (a) BOB-LPDAC, (b) BOC-LPDAC and (c) BOI-LPDAC electrodes.

The oxidation of LPDAC occurs at 495 °C and results in a weight loss of 89.79%.[64] In the case of the prepared nanocomposites, a substantial weight loss of 51.50% for BOB-LPDAC at 442 °C, 55.77% for BOC-LPDAC at 436 °C and 58.94% for BOI-LPDAC at 413 °C were noticed. A minimum weight loss of 51.50% and the supreme thermal stability of 442 °C suggest that BOB-LPDAC may act as a better electrode material than the other prepared bismuth oxyhalide electrodes for supercapattery energy storage applications.[65] The above findings can also be authenticated from electrochemical characterizations such as CV, GCD and EIS.

3.6 CV analysis

The charge storage mechanism of the prepared BOB, BOC, BOI, LPDAC, BOB-LPDAC, BOC-LPDAC and BOI-LPDAC electrodes was investigated using the cyclic voltammetry (CV) analysis. Where a three-electrode configuration was adopted. The potential window (ΔV) for BOB, BOC and BOI was in the range of -0.95 V to -0.2 V. For LPDAC, ΔV lies in the range of -0.5 V to 0.1 V, and for BOB-LPDAC, BOC-LPDAC and BOI-LPDAC, ΔV is in the range of -0.95 V to 0.1 V. In addition, the scan rate was in the range of 10–50 mV s^{-1} for all the cases.

The CV profiles of the BOB, BOC and BOI electrodes exhibit redox peaks due to faradaic reactions, which confirm the battery-type charge storage mechanism (see Fig. S12(a–c)).[66,67] Moreover, the existence of two anodic peaks, O1 and O2, authenticate the oxidation of Bi^0 into Bi^+ and Bi^+ into Bi^{3+}, respectively (see Table 1).[68,69] Furthermore, the presence of the cathodic peak (R1) is due to the reduction of Bi^{3+} to Bi^0.[68] When the scan rate increases, the oxidation peak may shift towards a positive potential and the reduction peak may shift towards a negative potential, resulting in an internal resistance drop in the prepared electrodes.[70] Also, at high scan rates, remarkable increments in both anodic and cathodic current densities were observed, which may due to the occurrence of (i) rapid interfacial faradaic redox reactions and (ii) fast electronic as well as ionic transport in the electrode.[67,71,72]

Fig. S12(d) shows the symmetrical and quasi-rectangular potential windows with no redox peaks, revealing the electric double layer capacitor (EDLC) behaviour of LPDAC.[73] Moreover, the EDLC nature of LPDAC confirms its porous nature that facilitates the efficient transport of electrolyte ions.[74] From Fig. 3(a–c), it is evident that the BOB-LPDAC, BOC-LPDAC and BOI-LPDAC electrodes have a more CV loop area and wider potential window than the bare BOB, BOC, BOI and LPDAC electrodes, respectively, owing to the synergistic effect of the battery- and capacitive-type charge storage mechanisms.[66,75]

Among all the electrodes, the BOB-LPDAC electrode exhibits the maximum current response of 93 mA due to its sheet-like morphology and higher surface area of 981 $m^2\ g^{-1}$ than BOC-LPDAC (82 mA) and BOI-LPDAC (65 mA) at 10 mV s^{-1}. Furthermore, transportation of more ions from LPDAC to BOB

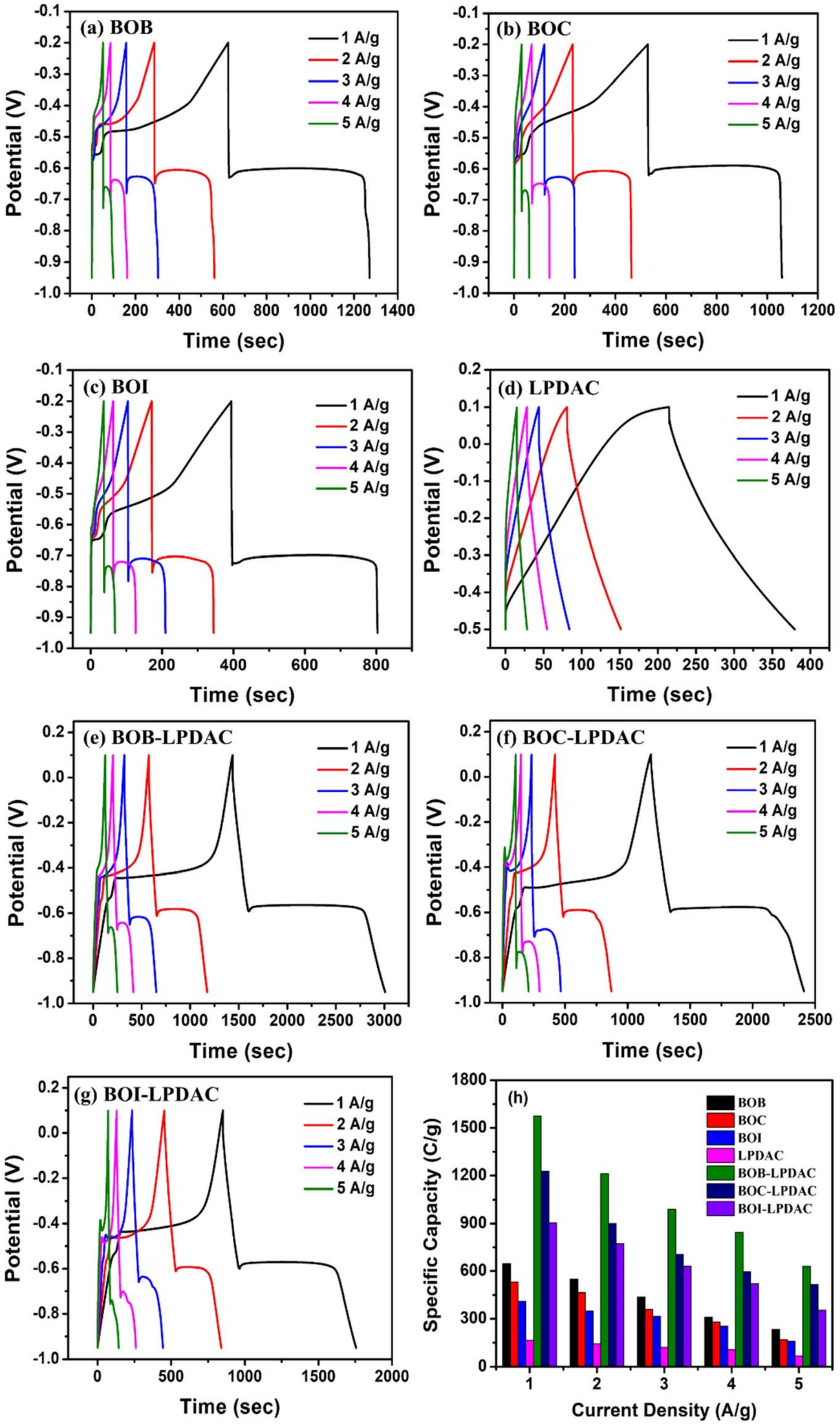

Fig. 4 (a–g) GCD profiles at different current densities and (h) specific capacity as a function of current density for the BOB, BOC, BOI, LPDAC, BOB-LPDAC, BOC-LPDAC and BOI-LPDAC electrodes.

is feasible.[75] The less current response in BOC-LPDAC and BOI-LPDAC may be attributed to their smaller surface area (783 m^2 g^{-1} and 610 m^2 g^{-1}) and irregular (nanosheet and nanoflake) morphology, respectively.[75] Hence, from the present CV analysis, it is clear that the prepared BOB-LPDAC nanocomposite may act as a better supercapattery electrode material than BOC-LPDAC and BOI-LPDAC.

3.7 GCD analysis

The electrochemical performance of the prepared BOB, BOC, BOI, LPDAC, BOB-LPDAC, BOC-LPDAC, and BOI-LPDAC

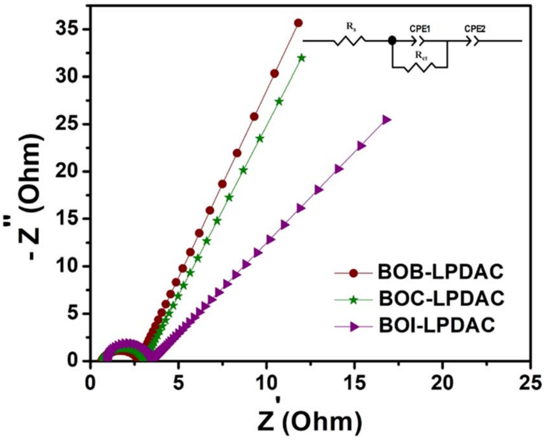

Fig. 5 Nyquist plots of BOB-LPDAC, BOC-LPDAC and BOI-LPDAC, along with the equivalent circuit model (inset).

electrodes was further studied by galvanostatic charge–discharge (GCD) analysis. The GCD profile of the BOB, BOC and BOI electrodes was attained in the potential window of −0.95 V to −0.2 V at different current densities of 1–5 A g^{-1} (see Fig. 4(a–c)). In addition, the discharge curve of the prepared BOB, BOC and BOI electrodes reveals an asymmetric shape with a two-step voltage disparity,[76] where the presence of a steep voltage drop (IR drop) is due to the internal resistance of the considered electrode materials and a prolonged plateau of voltage is owing to the reduction of Bi^{3+} into Bi (metal).[72,76] These properties indicate the battery-type charge storage mechanism in BOB, BOC and BOI due to their non-capacitive faradaic behaviour, which are consistent with the redox peaks in CV curves.[77,78]

In the case of LPDAC, the potential window is in the range of −0.5 V to 0.1 V. Moreover, it exhibits a triangular-shaped charge–discharge profile, which confirms the electric double layer capacitor-type charge storage mechanism (see Fig. 4(d)).[79] From Fig. 4(e–g), it is evident that the addition of LPDAC in BOB, BOC and BOI could extend the potential window in the range of −0.95 V to 0.1 V and greatly reduce the IR drop.[80] The decrement in the IR drop is due to the good electrical conductivity and high porous nature of LPDAC and thereby enhancements in the ion diffusion and electron transportation.[81] Fig. 4(h) shows the specific capacity (Q_S) of the prepared electrodes at various current densities (1–5 A g^{-1}). The calculated specific capacity of the prepared BOB, BOC, BOI, LPDAC, BOB-LPDAC, BOC-LPDAC, and BOI-LPDAC electrodes was found to be 646.75 C g^{-1}, 530.91 C g^{-1}, 409.57 C g^{-1}, 165.19 C g^{-1}, 1575.15 C g^{-1}, 1228 C g^{-1} and 905.37 C g^{-1} at a current density of 1 A g^{-1}, respectively. Furthermore, it is noticed that the specific capacity decreases with an increase in current density, which may due to the fast electrolytic ion transportation that restricts intercalation/deintercalation at the active sites of the electrodes during the electrochemical process.[67,82]

Compared to bare electrodes, the prepared BOB-LPDAC, BOC-LPDAC, and BOI-LPDAC nanocomposites exhibit high specific capacity and wider potential window due to their combined battery (BOX) and capacitive (LPDAC) type charge storage behaviour.[66] Among the prepared nanocomposites, BOB-LPDAC offers the maximum specific capacity of 1575.15 C g^{-1} due to its high surface area (981 m^2 g^{-1}), more pore volume (0.583 nm) and high porosity.[79] Moreover, these characteristics could offer more active sites for the electrolyte ions, which facilitate the abundant storage of charge in the prepared BOB-LPDAC.[83,84] Hence, from the present investigation, it is evident that the prepared BOB-LPDAC may serve as a better electrode material for supercapattery applications.

3.8 EIS analysis

The ion-transfer ability of the prepared BOB, BOC, BOI, LPDAC, BOB-LPDAC, BOC-LPDAC, and BOI-LPDAC electrodes was examined in the frequency range of 100 kHz–100 Hz at room temperature using the electrochemical impedance spectroscopy (EIS) analysis.[85] Fig. S13 and Fig. 5 illustrate the Nyquist plots of the electrodes, and the inset images depict the equivalent circuit model.

The calculated solution resistance (R_s) of the BOB, BOC, BOI, LPDAC, BOB-LPDAC, BOC-LPDAC, and BOI-LPDAC electrodes are 1.27 Ω, 1.37 Ω, 1.50 Ω, 1.01 Ω, 0.63 Ω, 0.72 Ω and 0.87 Ω, respectively (see Table S5). It authenticates that the reduction in R_s is due to addition of LPDAC in BOB/BOC/BOI, which further decreases the intrinsic resistance of the electrode materials and increases the electrical contact between the electrode material and the electrolyte ions.[86,87] Compared to all the prepared electrode materials, BOB-LPDAC exhibited the lowest R_{ct} of 2.12 Ω, which resulted in a rapid electrolyte ion transport at the electrode/electrolyte interface.[67,88] The low resistivity of BOB-LPDAC may be ascribed to its sheet-like morphology and large surface area (981 m^2 g^{-1}), providing shorter diffusion lengths.[86,88] In addition, the presence of more mesopores in BOB-LPDAC may act as ion reservoir channels, thereby promoting more intercalation and deintercalation of the electrolyte ions into the electrode.[67,86] Furthermore, it is observed that in the high to low frequency region of BOB-LPDAC, the imaginary part of impedance was almost linear, and this authenticates the coexistence of battery- and capacitive-type behaviours in the prepared BOB-LPDAC.[67]

4 Fabrication of the solid-state asymmetric (BOB-LPDAC‖LPDAC) and symmetric (BOB-LPDAC‖BOB-LPDAC) supercapattery devices

Based on the electrochemical performances obtained from the three-electrode cell configuration, BOB-LPDAC was further considered for the two-electrode cell configuration due to its maximum current response of 93 mA, supreme specific capacity of 1575.15 C g^{-1} and lower resistivity than the BOC-LPDAC and BOI-LPDAC electrodes. In the present work, the fabricated solid-state asymmetric (BOB-LPDAC‖LPDAC) and symmetric (BOB-LPDAC‖BOB-LPDAC) supercapattery devices were labelled as ASC and SSC, respectively. In both cases, the prepared PVA/KOH was utilised as the solid-state electrolyte. From the CV curves (see

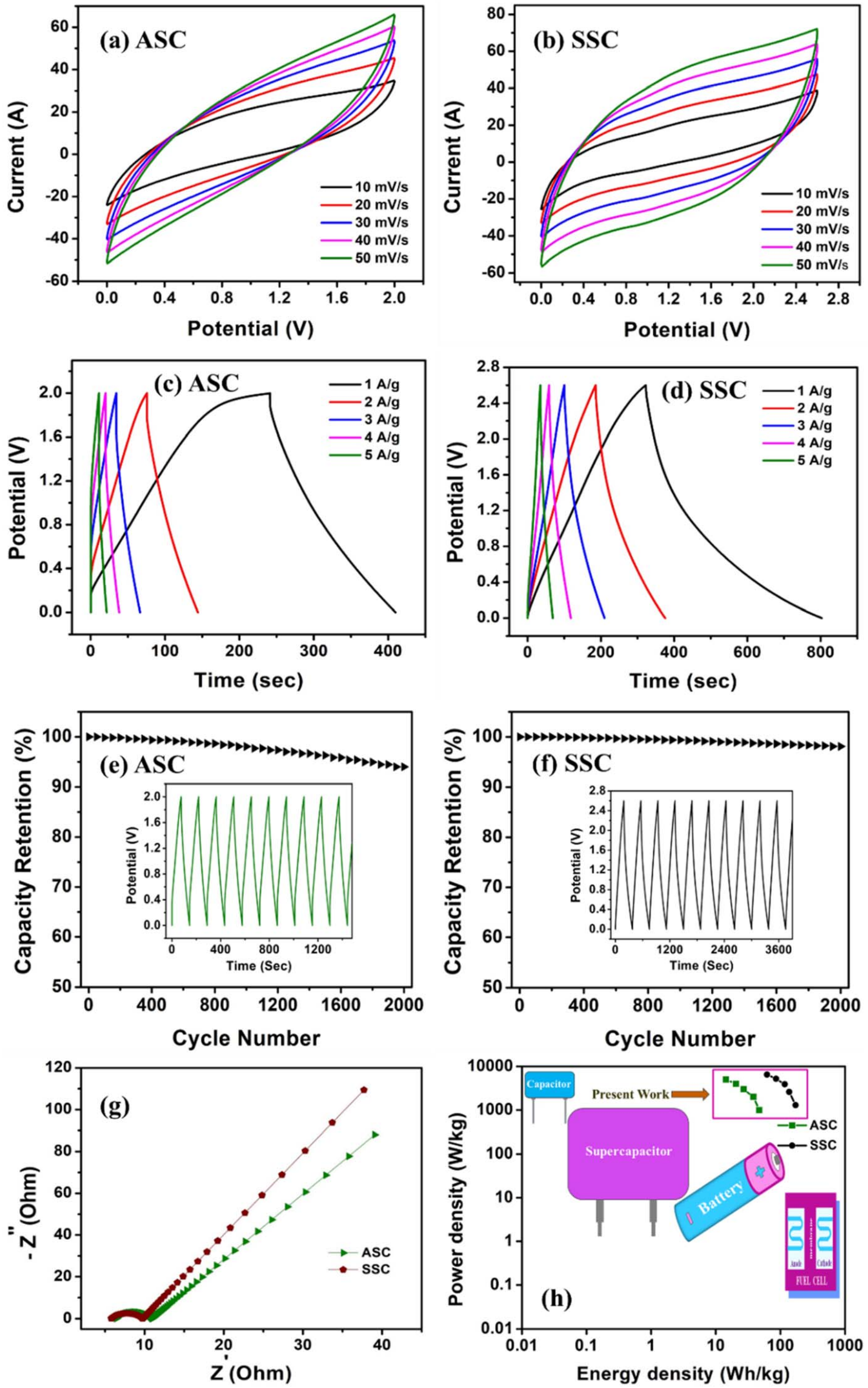

Fig. 6 (a and b) CV curves at different scan rates (10–50 mV s^{-1}), (c and d) GCD curves at different current densities (1–5 A g^{-1}), (e and f) cyclic stability (inset image shows the first ten charge–discharge cycles), (g) Nyquist plots and (h) Ragone plots of the ASC and SSC devices.

Fig. 6(a and b)), the ASC operates in the potential window of 0–2 V, and for SSC, the potential window was in the range of 0–2.6 V, respectively, where the scan rate varies from 10–50 mV s^{-1}. Compared to the ASC, the SSC has an enhanced CV loop area and high operating voltage.

The GCD profile of the ASC and SSC reveals triangular-shaped charge–discharge curves at a current density of 1–5 A g^{-1} (see Fig. 6(c and d)). The specific capacity (Q_S), energy density (E_D) and power density (P_D) of the prepared super-capattery devices are calculated using the following equations:[60,89]

$$Q_S(\mathrm{C\ g^{-1}}) = \frac{I \times \Delta t}{m} \tag{4}$$

Table 2 Comparison of the electrochemical energy storage performance of bismuth- and carbon-based electrodes

S. no.	Electrode materials	Electrolyte	ΔV (v)	E_D (Wh kg^{-1})	P_D (kW kg^{-1})	Current density (A g^{-1})	Capacity retention (%)	No. of cycles	Ref.	Type of energy storage applications
1	Bi_2O_3‖AC	KOH	1.9	18.24	1.008	—	83.67	1000	92	Supercapacitor
2	Bi_2O_3/FeS‖AC	KOH	1.2	15	0.59	1	88	7000	21	Supercapacitor
3	$BiMnO_3$‖AC	KOH	1.2	14.4	0.05	—	90	5000	20	Supercapacitor
4	$Bi_2Mo_3O_{12}$‖AC	KOH	1.5	47.5	0.75	1	71.9	10 000	1	Supercapacitor
5	$Bi_2Fe_2Mn_2O_{10}$‖AC	KOH	1.6	47.87	0.48	—	93.3	5000	2	Supercapacitor
6	BiOCl‖AC	KOH	1	17.2	0.251	0.5	82	3000	23	Supercapacitor
7	BiOCl/MXene‖BiOCl/MXene	KOH	1.2	15.2	0.567	—	85	5000	93	Supercapacitor
8	BiOCl‖BiOCl	KOH	1.5	21.8	0.773	0.5	—	—	69	Supercapacitor
9	BiOCl/MWCNT‖BiOCl/MWCNT	PVA/H_2SO_4	1	14.62	0.948	—	94	2000	94	Supercapacitor
10	SWCNT‖$BiPO_4$	KOH	1.5	02.2	0.68	0.4	84	10 000	95	Supercapacitor
11	NiO/CeO_2‖$Bi_{7\cdot47}Ni_{0.53}O_{11.73}$	KOH	1.5	78	0.201	—	94	2000	96	Supercapacitor
12	**BOB-LPDAC‖LPDAC**	PVA/KOH	2	47.1	1	1	94.01	2000	**Present work**	
				14.32	5	5				
13	**BOB-LPDAC‖BOB-LPDAC**	PVA/KOH	2.6	172.06	1.3	1	98.10	2000	**Present work**	
				62.13	6.5	5				

$$E_D(\text{Wh kg}^{-1}) = \frac{0.5 \times \Delta V \times Q_S}{3.6} \quad (5)$$

$$P_D(\text{W kg}^{-1}) = \frac{3600 \times E_D}{\Delta t} \quad (6)$$

where I is the applied current (A), Δt is the discharge time (s), m is the mass of the active material (g) and ΔV is the potential window (V). Eqn (4) is applicable only when the discharge curve is non-linear. Further, it assumes that the current is constant throughout the measurement, and mass is limited to only the active material on the electrode. Eqn (5) assumes a linear discharge and constant capacity throughout ΔV. It is applicable for a full supercapattery cell assembly. Its limitation is the assumption of linearity and dependence on discharge rates. However, eqn (6) determines stored energy over the discharge time and its limitation is in averaging performance.[90]

The calculated specific capacity for the ASC and SSC at a current density of 1 A g^{-1} was found to be 169.57 C g^{-1} and 476.46 C g^{-1}, respectively. In addition, the ASC has an energy density of 47.1 Wh kg^{-1} and a power density of 1 kW kg^{-1} at 1 A g^{-1}, while it delivers 14.32 Wh kg^{-1} of energy density and 5 kW kg^{-1} of power density at 5 A g^{-1} (see Table 2). But in the case of SSC, 172.06 Wh kg^{-1} of energy density and 1.3 kW kg^{-1} of power density were attained at 1 A g^{-1}. As the current density increases to 5 A g^{-1}, the power density increases (6.5 kW kg^{-1}) and energy density (62.13 Wh kg^{-1}) decreases. From the obtained E_D and P_D values, it is confirmed that the utilization of PVA/KOH as the solid-state electrolyte delivers superior electrochemical performances, and the fabricated ASC and SSC belong to a category between supercapacitor and battery in the Ragone plot (see Fig. 6(h)).

The cyclic stability of the ASC and SSC devices was tested for 2000 cycles at a current density of 2 A g^{-1} (see Fig. 6(e and f)), where the inset image represents the first ten consecutive charging and discharging cycles. Both the ASC and SSC devices could retain 94.01% and 98.10% capacity, respectively, even after 2000 cycles and resulted in excellent electrochemical robustness.[91] The Nyquist plot illustrates that the SSC has a lower charge transfer resistance (R_{ct}) of 3.96 Ω than that of ASC (4.53 Ω) which facilitates the fast transfer of ions in the SSC device (see Fig. 6(g)).[91]

Compared to the ASC, the SSC has a high specific capacity (476.46 C g^{-1}), wide potential window (0–2.6 V), more CV loop area, an outstanding energy density (172.06 Wh kg^{-1}), excellent power density (6.5 kW kg^{-1}), a less charge transfer resistance (3.96 Ω) and supreme capacity retention (98.10%). These remarkable properties of the SSC device, along with the highly porous nature of both the positive and negative electrodes (BOB-LPDAC), offer more diffusion and storage of ions during its electrochemical performance.

Table 2 summarises the comparison of the electrochemical performance of the fabricated ASC and SSC with previously reported bismuth- and carbon-based electrodes. When the positive electrode is either a metal (Fe) or non-metal (S) composite with bismuth oxide (Bi_2O_3) or Bi_2O_3 with a Bi atom replaced by a manganese (Mn) atom and the negative electrode is activated

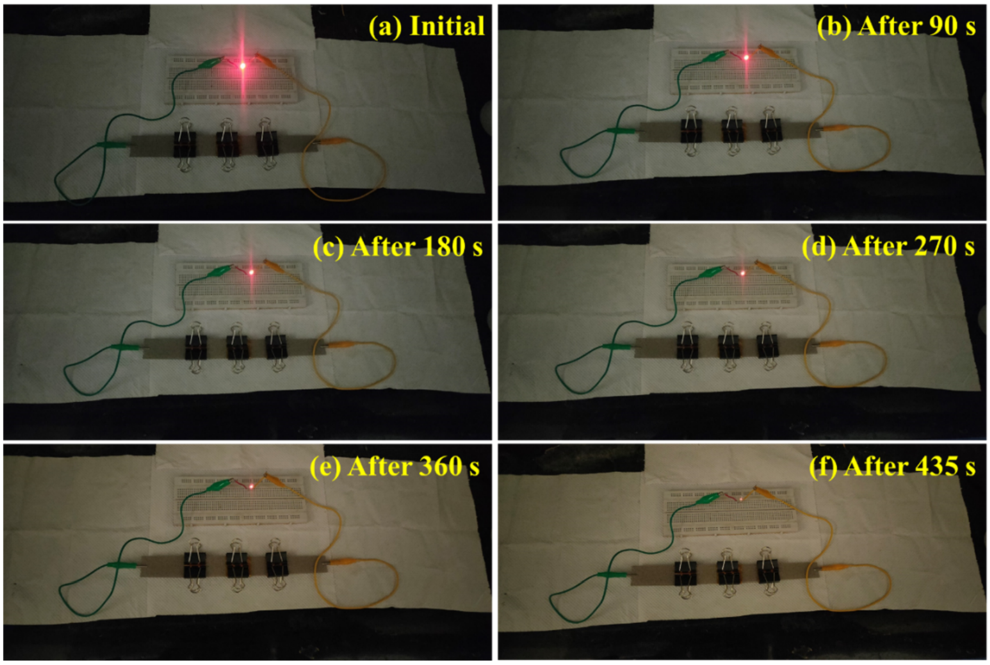

Fig. 7 Photographs of (a–f) two serially connected solid-state ASC devices lighting up a red LED for 435 s. (For the interpretation of the colours in this figure, the reader is suggested to refer to the web version of this article).

carbon (AC), both E_D and P_D decrease and the chemical stability of the devices is enhanced. In contrast, when bismuth oxide is doped with two or more transition metals (Mo, Fe and Mn), then E_D is greatly increased and P_D is reduced.

Moreover, the utilization of BiOCl as both the positive and negative electrodes and KOH as an electrolyte exhibits a high energy density and power density than AC and MXene-based devices. When a BiOCl/multi-walled carbon nanotube (MWCNT) served as both the positive and negative electrode and PVA/H_2SO_4 served as a gel electrolyte, the prepared device has more P_D and chemical stability and low E_D (14.62 Wh kg^{-1}) compared to bare BiOCl electrodes. Furthermore, there is a drastic decrease in E_D and P_D when single-walled carbon nanotube (SWCNT) is used as the positive electrode and bismuth phosphate ($BiPO_4$) is used as the negative electrode. Also, the fabrication of a supercapacitor device with a metal oxide-based material (NiO/CeO_2) as the positive electrode and a bismuth-based material ($Bi_{7.47}Ni_{0.53}O_{11.73}$) as the negative

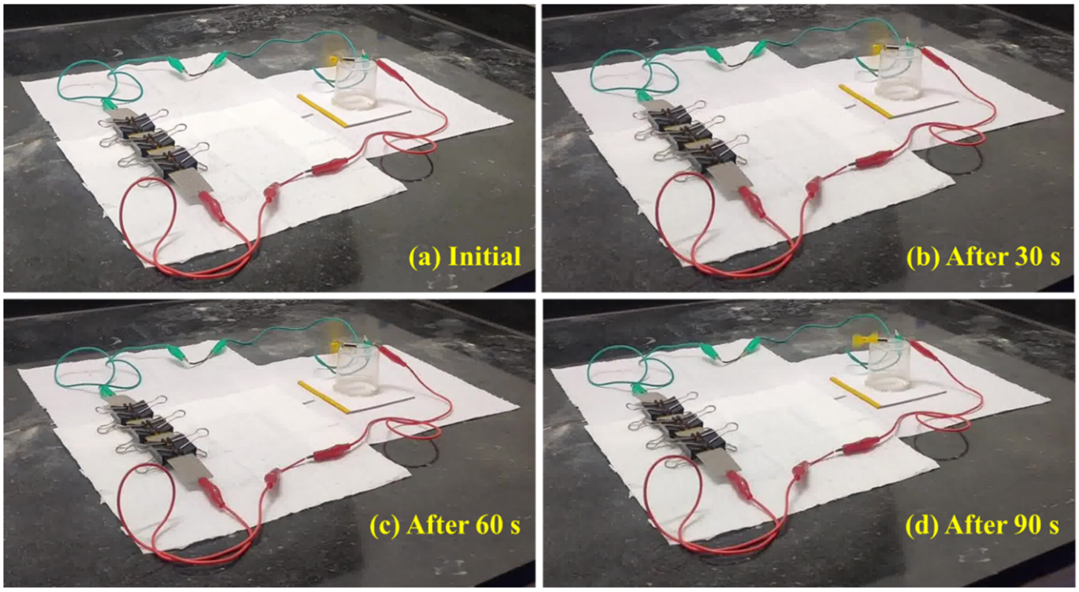

Fig. 8 Photographs of (a–d) two serially connected solid-state ASC devices powering an electrical motor fan (3.7 V) for 90 s.

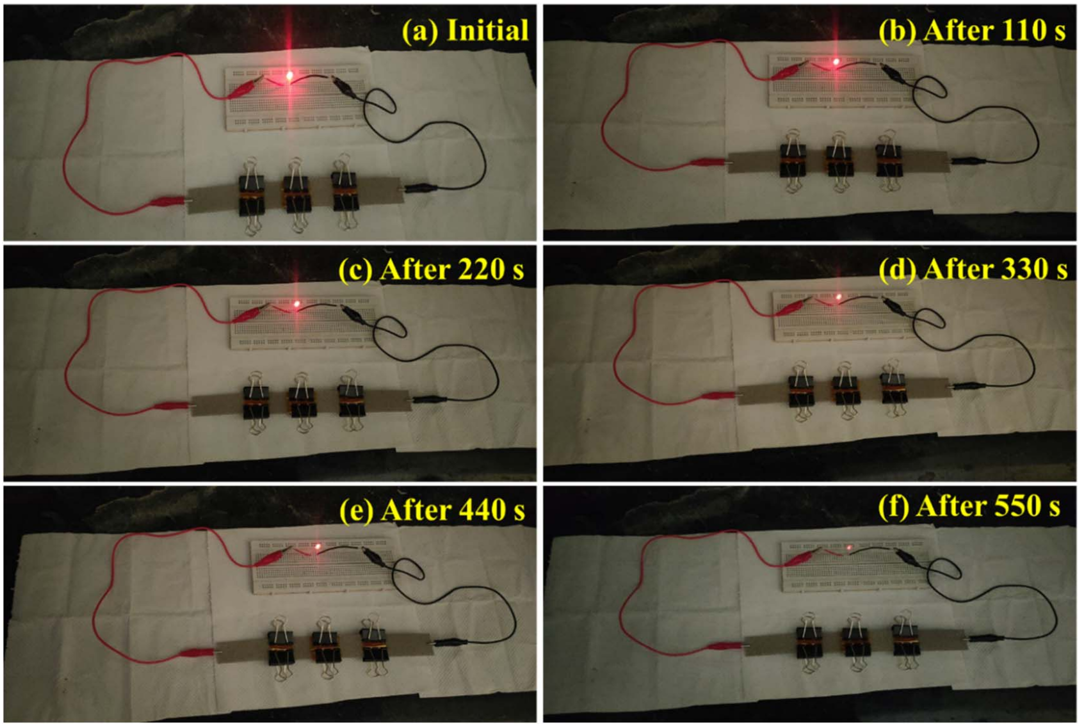

Fig. 9 Photographs of (a–f) two serially connected solid-state SSC devices lighting up a red LED for 550 s. (For the interpretation of the colours in this figure legend, the reader is suggested to refer to the web version of this article).

electrode yields a high E_D (78 Wh kg^{-1}) and moderate P_D (0.201 kW kg^{-1}).

From Table 2, it is clear that all the reported electrode materials exhibit either a low energy density or power density. But, the prepared SSC device delivers an ultrahigh energy density of 172.06 Wh kg^{-1}, a maximum power density of 6.5 kW kg^{-1}, high cell voltage of 2.6 V and cyclic stability of 98.10% compared with the other electrode materials. The remarkable electrochemical energy storage performance of the SSC is due to the utilization of PVA/KOH as the solid-state electrolyte and also the synergistic effects of battery-type faradaic and capacitive reaction provided by BOB and LPDAC, respectively.[66] Hence, the prepared BOB-LPDAC may serve as a prominent electrode material for the fabrication of advanced SSC devices in the realm of electrochemical energy storage applications in the near future.

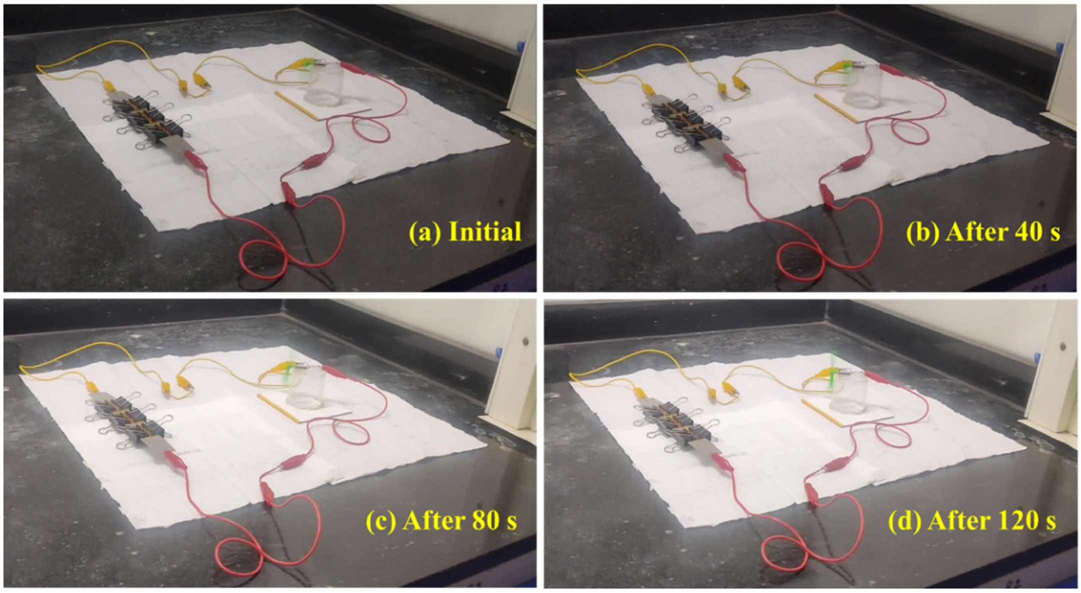

Fig. 10 Photographs of (a–d) two serially connected solid-state SSC devices powering an electrical motor fan (3.7 V) for 120 s.

5 Powering of a red LED and an electrical motor fan using the solid-state ASC and SSC devices

To examine the prepared ASC and SSC devices for practical applications, both the devices were charged for 1 min. The solid-state ASC device could light up a commercial red LED for 7 min 18 s (438 s) (see Fig. 7(a–f)), and the same device could power an electric motor fan for 1 min 31 s (91 s) (see Fig. 8(a–d)). The solid-state SSC device could light up a commercial red LED for 9 min 15 s (555 s) (see Fig. 9(a–f)) and an electric motor fan for 2 min 2 s (122 s) (see Fig. 10(a–d)).

From these results, it is observed that the prepared SSC device offers superior electrochemical performance than the ASC device. Hence, the prepared SSC device with a high operating potential (2.6 V), an outstanding energy density (172.06 Wh kg^{-1}) and excellent power density (6.5 kW kg^{-1}) may act as a potential power source in the near future.

6 Conclusions

In summary, three nanocomposites, namely, BOB-LPDAC, BOC-LPDAC and BOI-LPDAC, were successfully synthesized, and their applicability as electrode materials were tested using an electrochemical analysis. Among all, BOB-LPDAC exhibited a superior specific surface area of 981 m^2 g^{-1} than BOC-LPDAC (783 m^2 g^{-1}) and BOI-LPDAC (610 m^2 g^{-1}), thereby offering more adsorption sites to store more electrolyte ions. The enhanced electrochemical performance of these three electrodes than bare electrodes (BOB, BOC and BOI, respectively) may due to the presence of more CV loop area, a wider potential window and the synergistic effect (battery-type faradaic and capacitive reaction) offered by BOX and LPDAC in the nanocomposites. Based on the superior electrochemical performance, the BOB-LPDAC and LPDAC electrodes were alone utilized for the construction of supercapattery devices. The fabricated solid-state SSC device could deliver a high specific capacity of 476.46 C g^{-1} and an excellent power density of 6.5 kW kg^{-1} than the solid-state ASC device (169.57 C g^{-1} and 5 kW kg^{-1}). In addition, the fabricated ASC and SSC devices offered 94.01% and 98.10% capacity retention even after 2000 charge–discharge cycles. An outstanding specific capacity (476.46 C g^{-1}), cell voltage (2.6 V), energy density (172.06 Wh kg^{-1}), power density (6.5 kW kg^{-1}) and capacity retention (98.10%) suggested that the prepared BOB-LPDAC nanocomposite may serve as an efficient electrode material in the realm of solid-state symmetric supercapattery energy storage applications.

Author contributions

Bhuvaneshwari Ramasamy: writing – original draft, methodology, investigation. Jeya M. Peter Paul: visualization. Kannan Raman: validation, formal analysis. Rajashabala Sundaram: writing – review & editing, validation, supervision, resources, project administration, conceptualization.

Conflicts of interest

The authors declare that they have no known competing financial interests or personal relationships that could have appeared to influence the work reported in this paper.

Note from the Editor

This paper was published following the retraction of D5RA07844J. The authors of D5RA07844J published that paper without carrying out the work themselves, having had access to the original version of the paper as peer reviewers. D5RA07844J was subsequently retracted as the authors of that version could not prove that they had carried out the work. The retraction notice for this paper provides more details and can be accessed here: https://pubs.rsc.org/en/content/articlelanding/2026/ra/d6ra90026g This paper was peer reviewed independently following the retraction of D5RA07844J, and any overlap between the two papers should not be considered due to the situation described here.

Data availability

Data will be made available on request.

Supplementary information (SI) is available. See DOI: https://doi.org/10.1039/d6ra02955h.

Acknowledgements

The authors (SRS and RB) thank the Anusandhan National Research Foundation (ANRF) (EEQ/2022/000771) to carry out this research work.

References

1 B. Shunmughananthan, T. Dheivasigamani, J. Sthevan Kovil Pitchai and S. Periyasamy, *Dalton Trans.*, 2022, **51**, 15579–15592.
2 D. Ali, F. Ashiq, I. Muneer, H. M. Fahad, A. Waheed, M. Z. Butt, R. Ahmad and M. F. M. R. Wee, *Electrochim. Acta*, 2023, **464**, 142863.
3 K. Manoharan, V. K. Palaniswamy, K. Raman and R. Sundaram, *J. Alloys Compd.*, 2021, **860**, 158444.
4 V. S. Devi, K. Kannadasan, P. C. Sharafudeen and P. Elumalai, *New J. Chem.*, 2022, **46**, 15130–15144.
5 G. M, A. J, S. K. E and N. M, *Int. J. Hydrogen Energy*, 2025, **97**, 1212–1226.
6 O. Gerard, C. H. Khor, T. Prasankumar, S. Ramesh, K. Ramesh, S. K. Tiong and S. Ramesh, *J. Alloys Compd.*, 2025, **1034**, 181402.
7 B. Saravanakumar, X. Wang, W. Zhang, L. Xing and W. Li, *Chem. Eng. J.*, 2019, **373**, 547–555.
8 S. Korkmaz, *Fuel*, 2025, **391**, 134359.
9 S. Prabhu, M. Maruthapandi, A. Durairaj, S. A. Kumar, J. H. T. Luong, R. Ramesh and A. Gedanken, *Fuel*, 2023, **344**, 128122.

10 G. Surender, F. S. Omar, S. Bashir, M. Pershaanaa, S. Ramesh and K. Ramesh, *J. Energy Storage*, 2021, **39**, 102599.

11 Y. Li, Z. Luo, S. Liang, H. Qin, X. Zhao, L. Chen, H. Wang and S. Chen, *J. Mater. Sci. Technol.*, 2021, **89**, 199–208.

12 N. Tang, H. You, M. Li, G. Z. Chen and L. Zhang, *Nanoscale*, 2018, **10**, 20526–20532.

13 R. Velayutham, C. J. Raj, P. Thondaiman, A. M. Kale, R. Manikandan, J. D. Rodney, Y. Choi, Y. J. Lee, M. Kim, S. Moulton and B. C. Kim, *J. Mater. Sci. Technol.*, 2025, **228**, 155–171.

14 M. Saqib, A. Asghar, Z. Chen, A. A. Abdel Hafez, M. Y. A. Almashnowi, Q. Arshad, M. Y. Awaji, Y. Javad, M. Kuku and M. S. Rashid, *J. Alloys Compd.*, 2025, **1010**, 177986.

15 O. Gerard, A. Numan, M. A. A. M. Abdah, M. Khalid, S. Ramesh and K. Ramesh, *J. Energy Storage*, 2023, **61**, 106813.

16 E. Baasanjav, K. A. S. Raj, H. Hakkeem, C. S. Rout and S. M. Jeong, *J. Mater. Sci. Technol.*, 2025, **228**, 42–53.

17 K. Xu, L. Wang, X. Xu, S. X. Dou, W. Hao and Y. Du, *Energy Storage Mater.*, 2019, **19**, 446–463.

18 N. Devi and S. S. Ray, *Mater. Today Commun.*, 2020, **25**, 101691.

19 J. Chang, T. Wang, J. Ren, D. Wu, K. Jiang and Z. Gao, *J. Colloid Interface Sci.*, 2025, **681**, 229–238.

20 A. M. Teli, T. S. Bhat, S. A. Beknalkar, S. M. Mane, L. S. Chaudhary, D. S. Patil, S. A. Pawar, H. Efstathiadis and J. Cheol Shin, *Chem. Eng. J.*, 2022, **430**, 133138.

21 M. Shahzad, M. Li and D. Muhammad, *J. Mater. Sci. Eng. B*, 2025, **321**, 118493.

22 R. G. Bobade, N. B. Dabke, S. F. Shaikh, A. M. Al-Enizi, B. Pandit, B. J. Lokhande and R. C. Ambare, *Batter. Supercaps*, 2024, **7**, e202400163.

23 W. Hong, L. Wang, K. Liu, X. Han, Y. Zhou, P. Gao, R. Ding and E. Liu, *J. Alloys Compd.*, 2018, **746**, 292–300.

24 S. Palani, U. S. Veerasamy, Y. Mona, C. Chaichana, P. Suttakul, R. Wanison and R. Balu, *Diam. Relat. Mater.*, 2024, **148**, 111419.

25 J. Di, J. Xia, H. Li, S. Guo and S. Dai, *Nano Energy*, 2017, **41**, 172–192.

26 R. Manikandan, A. D. Savariraj, G. Nagaraju, A. M. Kale, J. Puigdollers, H. Park, H. S. Kim, J. M. Oh, C. J. Raj and B. C. Kim, *J. Mater. Sci. Technol.*, 2023, **157**, 220–233.

27 K. Manoharan, B. Ramasamy, K. Raman and R. Sundaram, *J. Energy Storage*, 2023, **70**, 107931.

28 K. Surya and M. S. Michael, *Biomass Bioenergy*, 2021, **152**, 106175.

29 M. D. Mehare, A. D. Deshmukh and S. J. Dhoble, *J. Mater. Sci.:Mater. Electron.*, 2021, **32**, 14057–14071.

30 T. Manimekala, R. Sivasubramanian, M. A. Dar and G. Dharmalingam, *RSC Adv.*, 2025, **15**, 2490–2522.

31 S. Ahmed, A. Ahmed and M. Rafat, *J. Energy Storage*, 2019, **26**, 100988.

32 L. Luo, Y. Lan, Q. Zhang, J. Deng, L. Luo, Q. Zeng, H. Gao and W. Zhao, *J. Energy Storage*, 2022, **55**, 105839.

33 X. Zhu, Y. Zeng, X. Zhao, D. Liu, W. Lei and S. Lu, *EcoEnergy*, 2025, **3**, e70000.

34 X. Lv, D. Y. S. Yan, F. L. Y. Lam, Y. H. Ng, S. Yin and A. K. An, *Chem. Eng. J.*, 2020, **401**, 126012.

35 L. Allagui, B. Chouchene, T. Gries, G. Medjahdi, E. Girot, X. Framboisier, A. B. haj Amara, L. Balan and R. Schneider, *Appl. Surf. Sci.*, 2019, **490**, 580–591.

36 K. S. Bhavsar, P. K. Labhane, R. B. Dhake and G. H. Sonawane, *Inorg. Chem. Commun.*, 2019, **104**, 134–144.

37 J. Chen, M. Guan, W. Cai, J. Guo, C. Xiao and G. Zhang, *Phys. Chem. Chem. Phys.*, 2014, **16**, 20909–20914.

38 F. Al Marzouqi, B. Al Farsi, A. T. Kuvarega, H. A. J. Al Lawati, S. M. Z. Al Kindy, Y. Kim and R. Selvaraj, *ACS Omega*, 2019, **4**, 4671–4678.

39 J. Li, F. Yang, Q. Zhou, L. Wu, W. Li, R. Ren and Y. Lv, *RSC Adv.*, 2019, **9**, 23545–23553.

40 Y. M. Xia, J. H. Zhang, M. Xia, Y. Zhao, S. P. Chu and W. W. Gao, *J. Mater. Sci.:Mater. Electron.*, 2020, **31**, 1996–2009.

41 R. Q. Miao, Z. H. He, B. T. Wu, J. Liu, S. W. Wang, K. Wang, W. Wang, L. Li and Z. T. Liu, *Chem. Eng. J.*, 2024, **481**, 148293.

42 Komal, A. Kumar, Y. Kumar and V. K. Shukla, *J. Mater. Sci.:Mater. Electron.*, 2023, **34**, 1880.

43 J. Hou, K. Jiang, M. Shen, R. Wei, X. Wu, F. Idrees and C. Cao, *Sci. Rep.*, 2017, **7**, 11665.

44 Y. Ao, H. Tang, P. Wang, C. Wang, J. Hou and J. Qian, *Compos. B Eng.*, 2014, **59**, 96–100.

45 S. Nethaji, G. Tamilarasan, P. Neehar and A. Sivasamy, *J. Environ. Chem. Eng.*, 2018, **6**, 3735–3744.

46 Z. Ali, M. Aadil, B. zainab, M. H. Rasool, W. Hassan, S. Mubarik, Z. Ahmad, N. A. Almuhous, A. A. Alothman and M. Hussain, *Inorg. Chem. Commun.*, 2023, **157**, 111399.

47 V. K. Palaniswamy, K. Raman and R. Sundaram, *Surf. Interfaces*, 2025, **72**, 107259.

48 M. Aadil, S. Zulfiqar, P. O. Agboola, M. F. Aly Aboud, I. Shakir and M. F. Warsi, *Synth. Met.*, 2021, **272**, 116645.

49 M. Arumugam and M. Y. Choi, *J. Ind. Eng. Chem.*, 2020, **81**, 237–268.

50 M. Singh, A. Kumar and V. Krishnan, *Mater. Adv.*, 2020, **1**, 1262–1272.

51 H. Weldekidan, H. Patel, A. Mohanty and M. Misra, *Carbon Capture Sci. Technol.*, 2024, **10**, 100149.

52 K. Manoharan, R. Sundaram and K. Raman, *Int. J. Hydrogen Energy*, 2023, **48**, 28694–28711.

53 Z. Oruç, M. Ergüt, D. Uzunoğlu and A. Özer, *J. Environ. Chem. Eng.*, 2019, **7**, 103231.

54 S. Song, W. Gao, X. Wang, X. Li, D. Liu, Y. Xing and H. Zhang, *Dalton Trans.*, 2012, **41**, 10472–10476.

55 Y. Peng, P. Kan, Q. Zhang and Y. Zhou, *Catalysts*, 2019, **9**, 558.

56 Q. Yang, H. Li, C. Feng, Q. Ma, L. Zhang, R. Wang, J. Liu, S. Zhang, T. Zhou, Z. Guo and C. Zhang, *Nanoscale*, 2022, **14**, 5814–5823.

57 A. Han, J. Sun, X. Lin, C. H. Yuan, G. K. Chuah and S. Jaenicke, *RSC Adv.*, 2015, **5**, 88298–88305.

58 T. Li, M. Aadil, S. Zulfiqar, A. Anwar, S. M. Yakout, N. M. Panduro-Tenazoa and S. Mubeen, *Ceram. Int.*, 2023, **49**, 27827–27836.

59 R. Arora, S. P. Nehra and S. Lata, *J. Energy Storage*, 2022, **56**, 105879.

60 A. U. Rehman, A. M. Afzal, M. W. Iqbal, M. Ali, S. M. Wabaidur, E. A. Al-Ammar, S. Mumtaz and E. H. Choi, *J. Energy Storage*, 2023, **71**, 108022.

61 M. U. Khalid, K. M. Katubi, S. Zulfiqar, Z. A. Alrowaili, M. Aadil, M. S. Al-Buriahi, M. Shahid and M. F. Warsi, *Fuel*, 2023, **343**, 127946.

62 A. C. Mera, C. A. Rodríguez, H. Valdés, A. F. Jaramillo, D. Rojas and M. F. Meléndrez, *Acta Chim. Slov.*, 2018, **65**, 429–437.

63 A. Kundu, S. Sharma and S. Basu, *J. Phys. Chem. Solids*, 2021, **154**, 110064.

64 M. Dadsetan, K. G. Latham, M. F. Khan, M. H. Zaher, S. Manzoor, E. R. Bobicki, M. M. Titirici and M. J. Thomson, *Carbon Trends*, 2023, **12**, 100277.

65 Y. Bao and K. Chen, *Appl. Surf. Sci.*, 2018, **437**, 51–61.

66 C. Murugan, K. Subramani, R. Subash, M. Sathish and A. Pandikumar, *Energy Fuels*, 2020, **34**, 16858–16869.

67 P. V. Shinde, N. M. Shinde, J. M. Yun, R. S. Mane and K. H. Kim, *ACS Omega*, 2019, **4**, 11093–11102.

68 L. Deng, Z. Ma, Z. huai Liu and G. Fan, *J. Alloys Compd.*, 2020, **812**, 152087.

69 Y. S. Thakur, A. D. Acharya, S. Sharma, Amisha, S. Bisoyi, Bhawna and S. S. Manhas, *Mater. Sci. Semicond. Process.*, 2024, **177**, 108376.

70 N. M. Shinde, Q. X. Xia, J. M. Yun, S. Singh, R. S. Mane and K. H. Kim, *Dalton Trans.*, 2017, **46**, 6601–6611.

71 Y. Arora, A. P. Shah, S. Battu, C. B. Maliakkal, S. Haram, A. Bhattacharya and D. Khushalani, *Sci. Rep.*, 2016, **6**, 36294.

72 Z. Khan, S. Bhattu, S. Haram and D. Khushalani, *RSC Adv.*, 2014, **4**, 17378–17381.

73 Y. Cheng, L. Wu, C. Fang, T. Li, J. Chen, M. Yang and Q. Zhang, *J. Mater. Res. Technol.*, 2020, **9**, 3261–3271.

74 H. B. M. Emrooz, M. S. Hosseini Naghavi, S. Mohammadi and S. M. Mousavi-Khoshdel, *J. Energy Storage*, 2022, **56**, 105989.

75 N. Joseph and A. C. Bose, *Electrochim. Acta*, 2019, **301**, 401–410.

76 A. Shameem, P. Devendran, A. Murugan, V. Siva, K. Seevakan, S. Hussain, D. Sivaganesh and S. Asath Bahadur, *J. Alloys Compd.*, 2023, **968**, 171825.

77 C. J. Raj, R. Manikandan, K. H. Yu, G. Nagaraju, M. S. Park, D. W. Kim, S. Y. Park and B. C. Kim, *Inorg. Chem. Front.*, 2020, **7**, 369–384.

78 Y. Hao, H. Guo, F. Yang, J. Zhang, N. Wu, M. Wang, C. Li and W. Yang, *J. Alloys Compd.*, 2022, **911**, 164726.

79 D. Shrestha, *Mater. Sci. Energy Technol.*, 2022, **5**, 353–365.

80 S. Kour, S. Tanwar and A. L. Sharma, *J. Alloys Compd.*, 2022, **910**, 164834.

81 F. Cheng, X. Yang, S. Zhang and W. Lu, *J. Power Sources*, 2020, **450**, 227678.

82 R. Ramachandran, W. Xuan, C. Zhao, X. Leng, D. Sun, D. Luo and F. Wang, *RSC Adv.*, 2018, **8**, 3462–3469.

83 S. Chandra Sekhar, G. Nagaraju, B. Ramulu and J. S. Yu, *Inorg. Chem. Front.*, 2019, **6**, 1707–1720.

84 I. Heng, F. W. Low, C. W. Lai, J. C. Juan, N. Amin and S. K. Tiong, *J. Alloys Compd.*, 2019, **796**, 13–24.

85 K. Nivedha and B. Subramanian, *J. Energy Storage*, 2023, **72**, 109269.

86 Lichchhavi, S. Kumar, A. K. Srivastava and S. K. Jha, *Electrochim. Acta*, 2023, **456**, 142438.

87 Z. Ahmad, A. Khalid, Z. M. Aldhafeeri, I. Barsoum, E. G. Hanna, M. Hasan, A. Anwar and M. Aadil, *J. Alloys Compd.*, 2024, **1002**, 175466.

88 A. Meftahi, M. Shabani-Nooshabadi and A. Reisi-Vanani, *Electrochim. Acta*, 2022, **430**, 141052.

89 F. Alam, M. Z. Iqbal, S. Alam and N. Alhassan, *J. Energy Storage*, 2021, **42**, 103150.

90 B. O. Okafor, I. S. Ike, I. I. Ayogu and T. C. Egbosiuba, *Next Mater.*, 2026, **11**, 101958.

91 Z. A. Shaikh, P. V. Shinde, S. F. Shaikh, A. M. Al-Enizi and R. S. Mane, *Solid State Sci.*, 2020, **102**, 106158.

92 S. A. Mane, A. A. Kashale, G. P. Kamble, S. S. Kolekar, S. D. Dhas, M. D. Patil, A. V. Moholkar, B. R. Sathe and A. V. Ghule, *J. Alloys Compd.*, 2022, **926**, 166722.

93 Q. X. Xia, N. M. Shinde, J. M. Yun, T. Zhang, R. S. Mane, S. Mathur and K. H. Kim, *Electrochim. Acta*, 2018, **271**, 351–360.

94 S. Dutta, S. Pal, D. Sikder and S. De, *J. Alloys Compd.*, 2020, **820**, 153115.

95 P. Kumari, S. K. Ghosh, V. K. Perla, C. Saha, H. Singh and K. Mallick, *J. Mater. Sci.:Mater. Electron.*, 2024, **35**, 1882.

96 J. Johnson William, I. Manohara Babu and G. Muralidharan, *Chem. Eng. J.*, 2021, **422**, 130058.